JOURNAL OF GEOPHYSICAL RESEARCH, VOL. 99, NO. B6, PAGES 11,705–11,722, JUNE 10, 1994

Seismic guided waves trapped in the fault zone of the Landers, California, earthquake of 1992

Yong-Gang Li, Keiiti Aki, David Adams, and Akiko Hasemi
Department of Earth Sciences, University of Southern California, Los Angeles

William H. K. Lee
U.S. Geological Survey, Menlo Park, California

Abstract. A mobile seismic array of seven stations was deployed at 11 sites along the fault trace of the $M7.4$ Landers earthquake of June 28, 1992, with a maximum offset of 1 km from the trace. We found a distinct wave train with a relatively long period following the S waves that shows up only when both the stations and the events are close to the fault trace. This wave train is interpreted as a seismic guided wave trapped in a low-velocity fault zone. To study the distribution of amplitude of the guided waves with distance from the fault trace and also their attenuation with travel distance along the fault zone, we eliminated source and recording site effects by the coda normalization method. The normalized amplitudes of guided waves show a spectral peak at 3–4 Hz, which decays sharply with distance from the fault trace. Spectral amplitudes at high frequencies (8–15 Hz) show an opposite trend, increasing with distance from the fault trace. The normalized amplitudes of guided waves at 3–4 Hz also show a systematic decrease with hypocentral distance along the fault zone, from which we infer an apparent Q of 50. In order to confirm the existence of the guided waves, a dense array of 31 stations was deployed at one of the 11 sites. The resultant records revealed unequivocal evidence for the existence of guided waves associated with the fault zone. By modeling the waveforms as S waves trapped in a low-velocity waveguide sandwiched between two homogeneous half-spaces with velocity $V_s = 3.0$ km/s, we infer a waveguide width of about 180 m, a shear velocity of 2.0–2.2 km/s, and a Q of ~50. Hypocenters of aftershocks with clear guided waves show a systematic distribution both laterally and with depth delineating the extent of the low-velocity fault zone in three dimensions. We find that the zone extends to a depth of at least 10 km. This zone apparently continues to the south across the Pinto Mountain fault because guided waves are observed at stations north of the Pinto Mountain fault for earthquakes with epicenters south of it. On the other hand, the zone appears to be discontinuous at the fault bend located about 20 km north of the mainshock epicenter; guided waves were observed for stations and epicenters which are located on the same sides of the fault bend but not for those on the opposite sides.

Introduction

As far as we know, seismic guided waves trapped in a fault zone were first discovered in a three-dimensional (3-D) vertical seismic profiling (VSP) experiment in the area surrounding a borehole drilled into fault zone of the Oroville, California, earthquake of 1975 [*Leary et al.*, 1987; *Li et al.*, 1987]. Records of borehole seismographs placed near the fault zone showed an unusually long-period wave train when the seismic source was within the fault zone. The characteristic waveform was attributed to a Love wave type mode trapped in a low-velocity, low-Q zone. Similar trapped modes were also identified in some of the borehole seismograms obtained at the San Andreas fault near Parkfield, California [*Li et al.*, 1990].

We believe that the study of fault zone trapped modes is important for several reasons. First, since the characteristics of trapped modes are determined directly by the mechanical properties of the fault zone, they may offer the most effective tool for monitoring the temporal change in fault zone properties for the purpose of earthquake prediction. Second, since the propagation of trapped modes is affected by the geometry of the fault zone at depth, they may offer information on the 3-D geometry of the fault zone, enabling us to find, for example, if the segmentation of fault traces observed on the surface persists to depth. The 3-D geometry of the fault zone will influence rupture propagation and may offer a basis for such elusive source parameters as the "asperities" and "barriers" proposed by seismologists for the strong ground motion prediction.

Finally, it is still a scientifically interesting and important practical question if there exists an upper bound frequency f_{max} of seismic waves that can be radiated from a fault zone; f_{max} is sometimes confusing and controversial because it could be attributed to source, path, recording site effects, or a combination of all three. *Brune* [1970] introduced a cutoff frequency of about 10 Hz in the acceleration spectrum in

Copyright 1994 by the American Geophysical Union.

Paper number 94JB00464.
0148-0227/94/94JB-00464$05.00

accordance with the general appearance of observed strong motion records. *Ida* [1973] interpreted the cutoff frequency as the source effect and estimated the critical slip in his slip-weakening model to be of the order of 10 cm. *Papageorgiou and Aki* [1983a, b] attributed the cutoff frequency to the size of cohesive zone (break down zone) acting as a spatial smoothing operator on fault slip. On the other hand, *Hanks* [1982] attributed f_{max} primarily to the local recording site effect, while *Anderson and Hough* [1984] attributed it to a strong effect of attenuation primarily at shallow depths below the recording station on high-frequency spectra. They attribute f_{max} to the site effect because they found that f_{max} depends on the site geology: lower for softer sediments and higher for harder rocks. *Su et al.* [1992], on the other hand, found that the site amplification factor increases monotonically with the decreasing geologic age of site up to 12 Hz, using the data from 132 stations of the U.S. Geological Survey (USGS) seismic network in central California. This means that the site-controlled f_{max} effect does not, on the average, apply to the frequency range up to 12 Hz.

Recently, *Kinoshita* [1992] demonstrated that the source-controlled f_{max} can vary from <10 to 40 Hz, depending on the earthquake source zone, using records from deep borehole seismographs placed in the basement rock in central Japan. This range of the source-controlled f_{max} may correspond to the range of cohesive zone size from 50 to >200 m based on the source model of *Papageorgiou and Aki* [1983a, b]. Since fault zone trapped modes arise from constructive interference of multiple reflections at the boundaries between the low-velocity fault zone and high-velocity surrounding rocks, the features of trapped waves (including amplitudes and frequency contents) are strongly dependent on the fault zone geometry and physical properties. We can resolve the fault zone width of tens to several hundreds of meters using the records of fault zone trapped mode. A simultaneous investigation of f_{max} and fault zone trapped modes may help to further clarifying the issue.

The Landers, California, earthquake of 1992 offered a wealth of data for studying various aspects of fault zone trapped modes. As we describe in the present paper, investigation of trapped modes reveals the physical properties and geometry of the fault zone along which they propagate.

Acquisition and Analysis of Data

Data Acquisition

From mid July to mid-August 1992, we deployed a mobile seismic array at 11 sites along the fault trace between Yucca Valley and Barstow to record aftershocks of the June 28 *M*7.4 Landers earthquake (Figure 1). The array consists of five six-channel Refraction Technology (REFTEK) instruments and seven Mark Products L4-C 1-Hz three-component sensors. Seven sensors were deployed across and parallel to the surface trace of the fault zone with a maximum distance of 1 km away from the fault trace at each site (see Figure 3 for the station configuration at site 8). Sensors were buried in shallow holes to avoid wind noise. We oriented the horizontal components parallel and perpendicular to the fault trace at each site. Five REFTEKs were synchronized to an external Nanometrics Omega clock system. Instrument operating parameters are shown in Table 1. Broadband FBA-23 (Kinemetrics trademark) accelerometers were used to record large ($M > 4$) aftershocks.

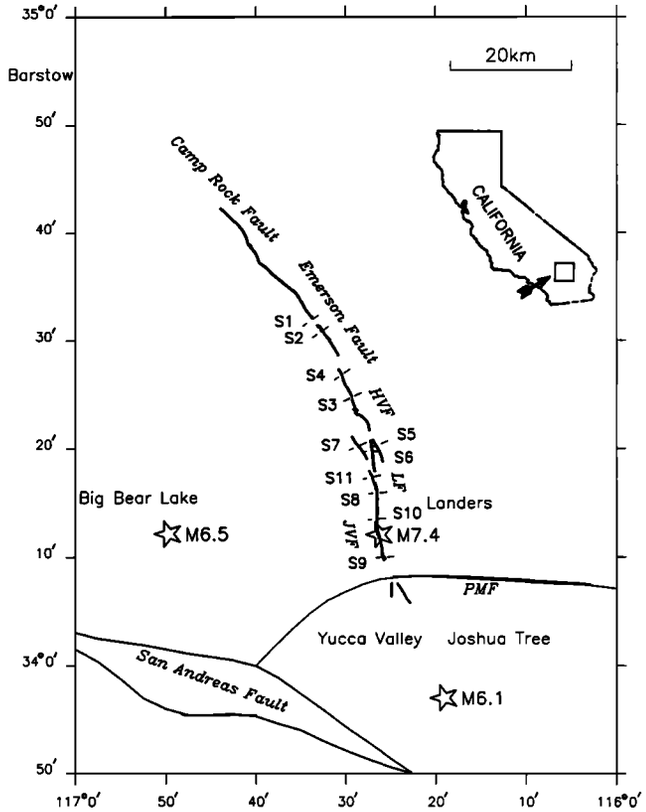

Figure 1. The map shows locations of 11 sites (S1–S11) where we set up a mobile seismic array (denoted by a dashed line) to record fault zone trapped waves. Stars show epicenters of the Joshua Tree, Landers, and Big Bear earthquakes of 1992. HVF, Homestead Valley Fault; JVF, Johnson Valley Fault; LF, Landers Fault; PMF, Pinto Mountain Fault. The inset shows the location of data collection area in California.

Instruments were tested at the beginning of the field experiment by deploying all seven sensors at a common site. The difference in amplitude spectrum among the seven channels (including the sensor and recording system) for a test event was less than 5%. We then set up the array at 11 sites along the fault trace of Landers earthquakes from Yucca Valley to the Camp Rock fault as shown in Figure 1. Instruments were operated for 1–2 days at each site, recording about 200 seismic events on the average. We recorded a total of about 2000 seismic events at the 11 sites. Figure 2 shows their epicenters according to the real time processing (RTP) catalog of the southern California seismic network.

We revisited site 8 in October 1992 with a dense array consisting of 31 sensors connected to a PC seismic data acquisition system [*Lee*, 1989] combined with REFTEK instruments. This was a joint project of the U.S. Geological Survey (USGS) and University of Southern California (USC). We present only preliminary results from this experiment. The main results described in this paper are from the data recorded at sites 3, 8, and 9, located 25 km north, 9 km north, and 2.5 km south of the Landers mainshock epicenter, respectively. A mainshock fault slip of 2.9 m was mapped on the ground at site 8. Between sites 3 and 8, the surface break of the fault zone is bent at an angle of 30° west of north. The Pinto Mountain fault intersects the rupture plane of the Landers earthquake at 3 km south of site 9 (Figure 1).

Outline of Data Processing and Analysis

Field data were transferred from the REFTEK internal 200 Mbytes hard disks to 8-mm tapes using a portable EXABYTE tape driver, and then transmitted to Sun computer stations for data processing. Data were processed in the following steps: (1) eliminating seismograms with any recording problems such as glitches, saturation, large noises, overlapping (two earthquakes occurred in a very short time interval), or truncation (recording terminated too early to include coda waves used for the normalization procedure described later); (2) low-pass filtering to eliminate 60-Hz electric noises if necessary; (3) locating events using the relocated seismic network catalog or using P and S arrival times and polarizations registered at the seven-station mobile array; (4) eliminating seismic events located too far away from the fault zone to excite trapped wave energy or to be used for study of seismic attenuation related to the fault zone; (5) selecting the time window in which we find relatively long-period wave trains closely following S waves; (6) calculating the amplitude spectrum of these waves in the selected time window and the amplitude spectrum of coda waves in a fixed time window with the same window length starting at 14 s from the earthquake origin time; (7) calculating the amplitude spectral ratio of trapped waves to coda waves for normalization to common source and receiver site condition; (8) plotting the coda-normalized spectral ratio of trapped waves versus station offset from the fault trace and also versus distance between source and receiver; and (9) simulating the trapped mode waveform to fit observations in terms of a structural waveguide model for determination of the width, velocity, and Q value of the fault zone.

The data processing and analysis were carried out on the Sun computer using academic software including PASSCAL Field Computer Subroutines developed by the PASSCAL Instrument Center, Seismic Analysis Code (SAC) developed by Lawrence Livermore National Laboratory and our own computer programs.

Table 2 shows the locations, magnitudes, and origin times of aftershocks recorded at sites 8, 9, and 3 for analysis of fault zone trapped waves in this study.

Spectral Analysis and Normalization by the Coda Method

In the analysis of the trapped mode recorded at site 8, we calculated the amplitude spectra for a 2-s time window (including 512 samples for Fourier transformation) starting from the S arrival using a Hanning window with 20-ms edge length. We found that this time window is adequate for analyzing fault zone trapped waves for events with their epicenters less than 15 km away from the recording array. We also found that the epicentral distance range of 5–15 km is most favorable to observe trapped waves. If the distance is shorter, the mode is not yet well developed in comparison to S waves, and if the distance is greater, the attenuation due to the low-Q fault zone tends to obscure it. This distance range was also used in our earlier observations of the fault zone trapped mode on the San Andreas fault near Parkfield [*Li et al.*, 1990].

The coda normalization procedure at steps 6 and 7 is based on the fundamental separability of source, path, and site effects in coda waves as well established empirically by *Aki* [1969] and later studies [e.g., *Chouet*, 1976; *Tucker and King*, 1984; *Phillips*, 1985]. The power spectrum of coda waves at a lapse time t measured from the earthquake origin time for frequency ω can be expressed as

$$P(\omega|t) = S(\omega)R(\omega)C(\omega|t),$$

where $S(\omega)$, $R(\omega)$, and $C(\omega|t)$ are source factor, receiver factor, and coda wave factor, respectively. $S(\omega)$ depends only on the earthquake source, $R(\omega)$ only on the recording site, and $C(\omega|t)$ is common to all sources and receivers as

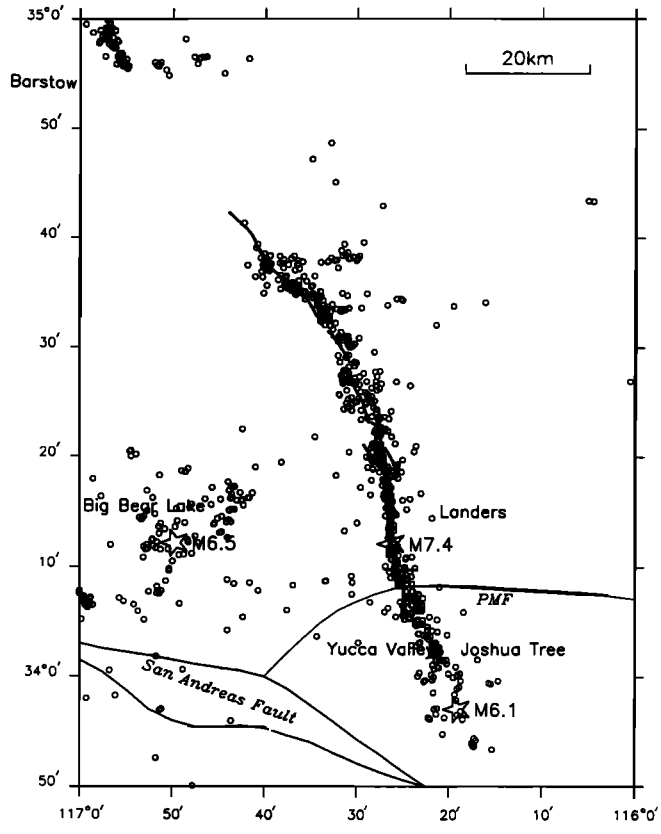

Figure 2. The map shows epicenters of about 1000 aftershocks of the Landers and Big Bear earthquakes that have been located by the USGS/California Institute of Technology seismic network during mid-July to mid-August, 1992. Stars show epicenters of the Joshua Tree, Landers, and Big Bear earthquakes of 1992.

Table 1. Instrument Parameters Used in the Experiment at Landers

Parameter	Description
Trigger mode	event
Channels	1–3 for L4-C sensor 4–6 for L4-C or FBA sensor
Minimum trigger channels	any two of channels 1, 2, 3
Sample rate	250 samples/s
Preamplifier	8 counts/±32,000 counts for L4-C 1 count/±32,000 counts for FBA
Recording length	60 s
Pretrigger length	10 s
Short-term average length	0.25 s
Long-term average length	30 s
Trigger ratio (LTA/STA)	10

Table 2. Locations, Times, and Magnitudes of Events Exciting Trapped Waves

Event	Origin Time, UT	Latitude	Longitude	Magnitude	Depth	Catalog
			July 17, 1992			
1	0540	34°15.67′	116°26.50′	···	5.5	USC
2	0553	34°16.50′	116°26.50′	···	4.9	USC
3	0601	34°13.20′	116°25.36′	···	6.3	CIT
4	0607	34°16.60′	116°27.50′	···	4.5	USC
5	0616	34°08.96′	116°23.92′	2.2	9.8	CIT
6	0623	34°16.30′	116°26.57′	···	4.3	USC
7	0646	34°10.50′	116°25.50′	···	7.0	USC
8	0654	34°10.66′	116°25.50′	···	7.0	USC
9	0803	34°19.69′	116′25.69′	1.2	5.7	CIT
10	0815	34°17.30′	116°26.50′	···	6.0	USC
11	0844	34°15.70′	116°26.47′	1.1	9.2	USC
12	1113	34°17.66′	116°26.97′	1.9	6.3	CIT
13	1143	34°09.14′	116°25.62′	2.2	10.5	CIT
14	1151	34°08.90′	116°27.83′	1.5	6.0	CIT
15	1217	34°21.85′	116°27.56′	2.1	6.1	CIT
16	1238	34°13.55′	116°26.16′	2.3	7.0	CIT
17	1426	34°15.50′	116°26.63′	2.9	5.5	CIT
18	1527	34°22.19′	116°28.16′	1.8	6.1	CIT
19	1539	34°16.67′	116°26.50′	0.7	5.5	CIT
20	1542	34°13.46′	116°26.52′	2.3	10.6	CIT
21	1609	34°09.62′	116°25.78′	2.4	8.4	CIT
22	1623	34°19.86′	116°27.30′	2.4	4.5	CIT
23	1637	34°10.30′	116°25.58′	2.0	7.0	CIT
24	1639	34°18.99′	116°26.39′	2.0	6.1	CIT
			July 30, 1992			
25	0534	34°16.87′	116°26.81′	···	3.9	USC
26	0804	34°05.99′	116°24.33′	2.1	4.5	CIT
27	0808	34°13.26′	116°25.94′	1.3	8.0	CIT
28	0901	34°05.15′	116°21.24′	1.4	6.0	CIT
29	0921	34°17.71′	116°26.99′	···	6.2	USC
30	0933	34°16.09′	116°26.29′	2.2	6.9	CIT
31	0935	34°17.14′	116°26.69′	···	6.3	USC
32	0955	34°17.17′	116°26.77′	···	4.5	USC
33	1028	34°14.60′	116°26.84′	···	6.1	USC
34	1040	34°15.31′	116°26.79′	···	5.2	USC
35	1040	34°17.24′	116°26.49′	···	6.3	USC
36	1113	34°15.91′	116°26.07′	1.7	5.8	CIT
37	1124	34°16.78′	116°26.85′	···	6.1	CIT
38	1124	34°18.57′	116°26.77′	···	6.0	USC
39	1226	34°17.38′	116°26.58′	···	4.8	USC
40	1653	34°03.19′	116°20.56′	1.6	7.9	CIT
41	1741	34°10.41′	116°25.83′	2.0	3.8	CIT
42	1933	34°15.60′	116°26.24′	···	5.1	USC
43	1936	34°16.20′	116°26.24′	2.1	6.3	CIT
44	2106	34°07.47′	116°24.74′	3.0	1.0	CIT

Table 2. (continued)

Event	Origin Time, UT	Latitude	Longitude	Magnitude	Depth	Catalog
			July 31, 1992			
45	0412	34°07.04′	116°24.17′	1.0	7.5	CIT
46	0424	34°08.27′	116°24.24′	2.3	5.9	CIT
47	0455	34°10.49′	116°26.40′	1.5	9.6	CIT
48	0508	34°04.62′	116°22.50′	···	5.0	CIT
49	0516	34°06.03′	116°23.41′	1.7	6.0	CIT
50	0553	34°03.85′	116°22.08′	···	3.9	CIT
51	0555	34°03.66′	116°21.97′	1.2	8.2	CIT
52	0612	34°08.73′	116°24.35′	1.4	6.0	CIT
53	0620	34°02.37′	116°21.21′	2.9	1.3	CIT
54	0753	34°00.89′	116°21.22′	2.8	5.2	CIT
55	0753	33°58.54′	116°21.64′	2.8	6.0	CIT
56	0803	34°00.83′	116°21.14′	2.5	3.8	CIT
57	0807	34°00.80′	116°21.04′	2.3	4.4	CIT
58	0922	34°08.92′	116°25.38′	···	5.0	CIT
59	0939	34°01.50′	116°20.88′	2.2	5.0	CIT
60	0939	34°06.24′	116°23.04′	2.3	6.0	CIT
61	1027	34°13.76′	116°25.93′	2.2	8.0	CIT
62	1048	34°21.42′	116°27.93′	2.3	6.0	CIT
63	1057	34°11.88′	116°25.53′	···	7.0	CIT
64	1127	34°06.41′	116°23.80′	1.6	9.1	CIT
65	1138	34°09.72′	116°25.72′	2.3	5.3	CIT
66	1138	34°09.72′	116°25.72′	2.3	5.3	CIT
67	1221	34°16.45′	116°25.25′	1.4	6.0	CIT
68	1415	34°10.72′	116°24.65′	2.0	13.5	CIT
69	1447	34°06.51′	116°23.00′	···	5.0	CIT
70	1655	34°02.89′	116°21.51′	1.9	6.0	CIT
71	1722	34°03.88′	116°22.18′	1.7	6.0	CIT
72	1739	34°06.77′	116°24.40′	···	5.0	CIT
73	1803	34°06.83′	116°24.40′	3.5	2.4	CIT
74	1821	34°06.43′	116°24.96′	2.9	2.1	CIT
			August 5, 1992			
75	2229	34°26.77′	116°30.14′	2.4	2.4	CIT
76	2332	34°25.49′	116°29.10′	1.9	7.6	CIT
			August 6, 1992			
77	0525	34°30.83′	116°31.60′	2.7	2.6	CIT
78	0526	34°30.89′	116°31.72′	2.3	9.0	CIT
79	0544	34°27.66′	116°30.71′	1.2	10.0	CIT
80	0552	34°29.87′	116°31.22′	1.3	1.0	CIT
81	0558	34°28.79′	116°30.67′	2.4	2.1	CIT
82	0622	34°28.14′	116°30.74′	2.1	6.0	CIT
83	0824	34°33.46′	116°33.49′	2.8	6.1	CIT

CIT and USC indicate the event located by the USGS/CIT seismic network and the seven-station mobile array, respectively. July 17 and 30, 1992, events were recorded at site 8; July 31, 1992, events were recorded at site 9; August 6 and 7, 1992, events were recorded at site 3.

long as the beginning of the coda time window is taken to be longer than about twice the S wave travel time from the source to receiver. In our case, the beginning of the coda window was taken at 14 s measured from the earthquake origin time, thus allowing source-receiver pairs within about 20 km for normalization. The normalization assumes that both the $S(\omega)$ and $R(\omega)$ are common between the trapped modes and the coda waves. This assumption may be approximately justified because both are primarily composed of S waves. By this normalization, we can eliminate the local site effect due to surface geology, and we also can combine data from different events for measuring the attenuation. The small scatter of normalized amplitude versus distance (Figure 6) demonstrates the power of this normalization procedure (also see *Mayeda et al.* [1992] for examples of this normalization).

Results of Analysis

Evidence for the Trapped Mode at Site 8

Station locations at recorder site 8 are shown in Figure 3. We carried out a preliminary experiment there in mid-July using three REFTEKs with three L4-C sensors deployed along the fault zone at GA, GB, and GC. Locations of the three stations were measured by Global Positioning System (GPS) at latitudes of 34°18.39′, 34°16.82′, 34°16.37′ and longitudes of 116°26.75′, 116°26.49′, 116°26.48′, respectively. We then deployed seven REFTEKs across the fault trace at G1–G7 in late July. We recorded about 400 events at site 8. We found clear evidence for fault zone trapped waves from 44 events occurring within the fault zone (see locations of these events in Table 2).

Figure 4 (top) shows seismograms from an aftershock (event 43 in Table 2) recorded at stations G1–G6 and the coda-normalized amplitude spectra in the 2-s time window after the beginning of the S wave. This event is located by the regional seismic network with the epicenter near the mainshock fault trace. The opposite polarities of the first arrivals registered at stations located on the east and west side of the array deployed across the fault trace may also support a location within the fault zone. In a laterally heterogeneous planar fault zone, the head wave refracted from the higher velocity wall rocks could arrive earlier than direct waves traveling in the slower-velocity wall rocks on the other side of the fault zone, as, for example, at the San Andreas fault near Parkfield [*Ben-Zion and Aki*, 1990]. However, in the case of the fault zone at Landers, which is embedded in a basement without obvious difference between the two wall rocks, the polarities of the first P motions should not be effected by head waves.

Figure 4 shows relatively long-period wave trains with slight dispersion closely following S waves at stations G2–G5, located close to the mainshock fault trace, more clearly than at stations G1 and G6, located farther from the fault trace. Station G3, located closest to the mainshock fault trace, registered the maximum normalized spectral amplitude of these wave trains at frequencies in which the trapped mode is dominant, about 4 Hz. The spectral peak amplitude at 2–5 Hz decreases rapidly as the station offset from the fault trace increases. On the other hand, the high-frequency waves in the frequency range from 8 to 15 Hz are more strongly attenuated at stations close to the mainshock fault trace than stations with greater offsets. These relatively long-period wave trains observed near the fault zone of the

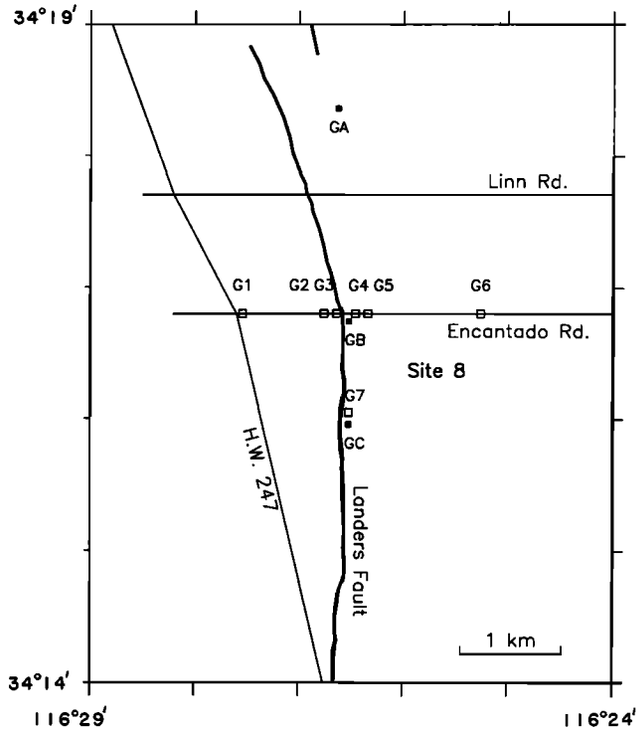

Figure 3. The map shows locations of mobile array stations at site 8. Stations GA, GB, and GC (solid squares) were set up in our preliminary experiment while G1–G7 (open squares) were set up for recording additional events. GA, GB, and GC are located 500 m, 50 m, and 100 m east of the mainshock fault trace. G1–G6 are located at 1 km west, 100 m west, 0, 100 m east, 200 m east, and 1 km east from the fault trace, respectively.

Landers earthquake show features similar to the fault zone trapped waves reported earlier for the San Andreas fault near Parkfield [*Li et al.*, 1990]. These observations suggest that a low-velocity, low-Q zone exits along the rupture plane of the Landers earthquake.

In contrast, the event occurring outside the fault zone and shown at the bottom of Figure 4, shows no evidence of a trapped mode. This event is located by the regional seismic network at a depth of 6 km and with the epicenter on the west of site 8, 3 km away from the fault trace. We did not observe the relatively long-period wave trains following the S waves from this event at any one of our stations. The normalized spectra are similar among all six stations, showing no spectral peaks at frequencies lower than 5 Hz.

Figure 5 illustrates additional examples of fault zone trapped waves from three aftershocks (event 30, 27, and 26 in Table 2) with various hypocentral distances (about 6.5 km, 10.3 km, and 18 km from site 8, respectively). Trapped waves were clearly recorded at stations G2–G5 near the mainshock fault trace, while they were not apparent at stations G1 and G6 far away from the fault zone. The peak amplitude of the normalized spectrum of trapped waves in the 2–5 Hz range decreases systematically with the station offset from the fault zone. We again found strong attenuation of high-frequency (8–15 Hz) seismic waves within the fault zone as compared to outside. We also found that the peak amplitude of the normalized spectrum of trapped waves decreases as the distance between the event and receiver increases.

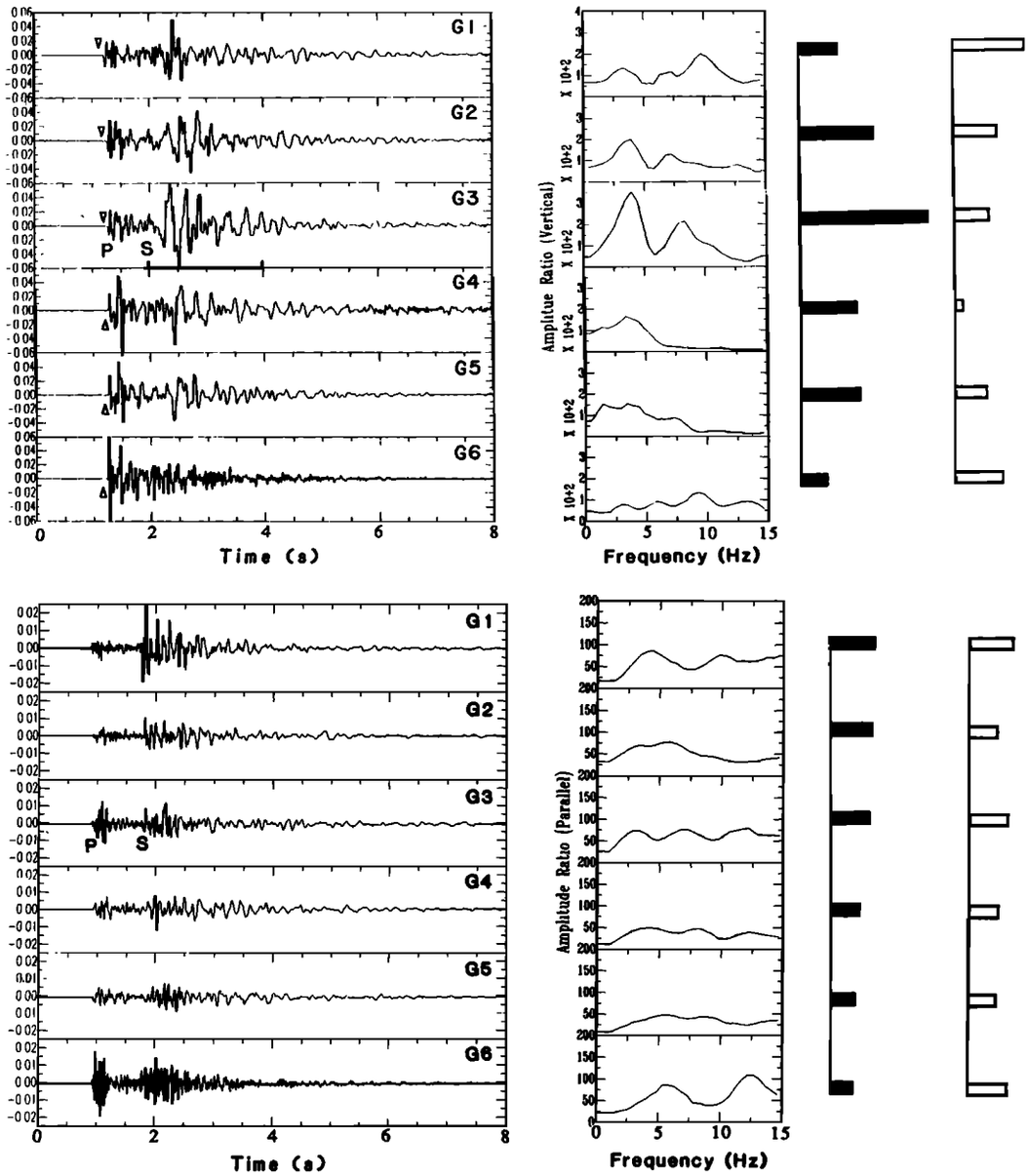

Figure 4. (Top) Vertical components of seismograms recorded at stations G1–G6 at site 8 for event 43 occurring within the fault zone. The open arrow indicates the polarity of the first *P* motion. (bottom) Horizontal components (parallel to the mainshock trace) of seismograms recorded at site 8 for an event occurring outside the fault zone. The bracket denotes a 2-s window starting from the *S* arrival and including the trapped mode. The normalized amplitude spectra are shown at the right of the seismograms. The solid bar represents the spectral peak in the frequency range 2–5 Hz. The open bar gives the average spectral amplitude in the frequency range 8–15 Hz. The bar chart is plotted in a fixed amplitude scale of 200.

In order to study the attenuation of trapped modes quantitatively, we plotted the peak amplitude of normalized spectra of trapped waves for 12 aftershocks occurring within the fault zone as a function of station offset from the mainshock fault trace (Figure 6, left) as well as a function of hypocentral distance (Figure 6, right). We found that the maximum amplitude of spectral peak appears at G3 (or G4) located closest to the mainshock fault trace and decays rapidly as the offset from the fault trace increases. We also found that the amplitude of the spectral peak at G3 (or G4) systematically decreases with the hypocentral distance r. Assuming a shear velocity of 2.0 km/s and that the spectral amplitude of trapped mode decays with $r^{1/2}$, we estimate $Q = 50$ at the frequency of 4 Hz. Since the measured Q value may be affected by the contamination of other phases, such as direct *S* waves [see *Ben-Zion and Aki*, 1990], more complete analysis requires a simultaneous simulation of *S* waves and trapped modes. However, because the *S* waves decay more quickly (proportional to distance r) than trapped waves (proportional to $r^{1/2}$) as they propagate along the fault zone, the effects of *S* waves on the Q value estimate are diminished as the distance increases.

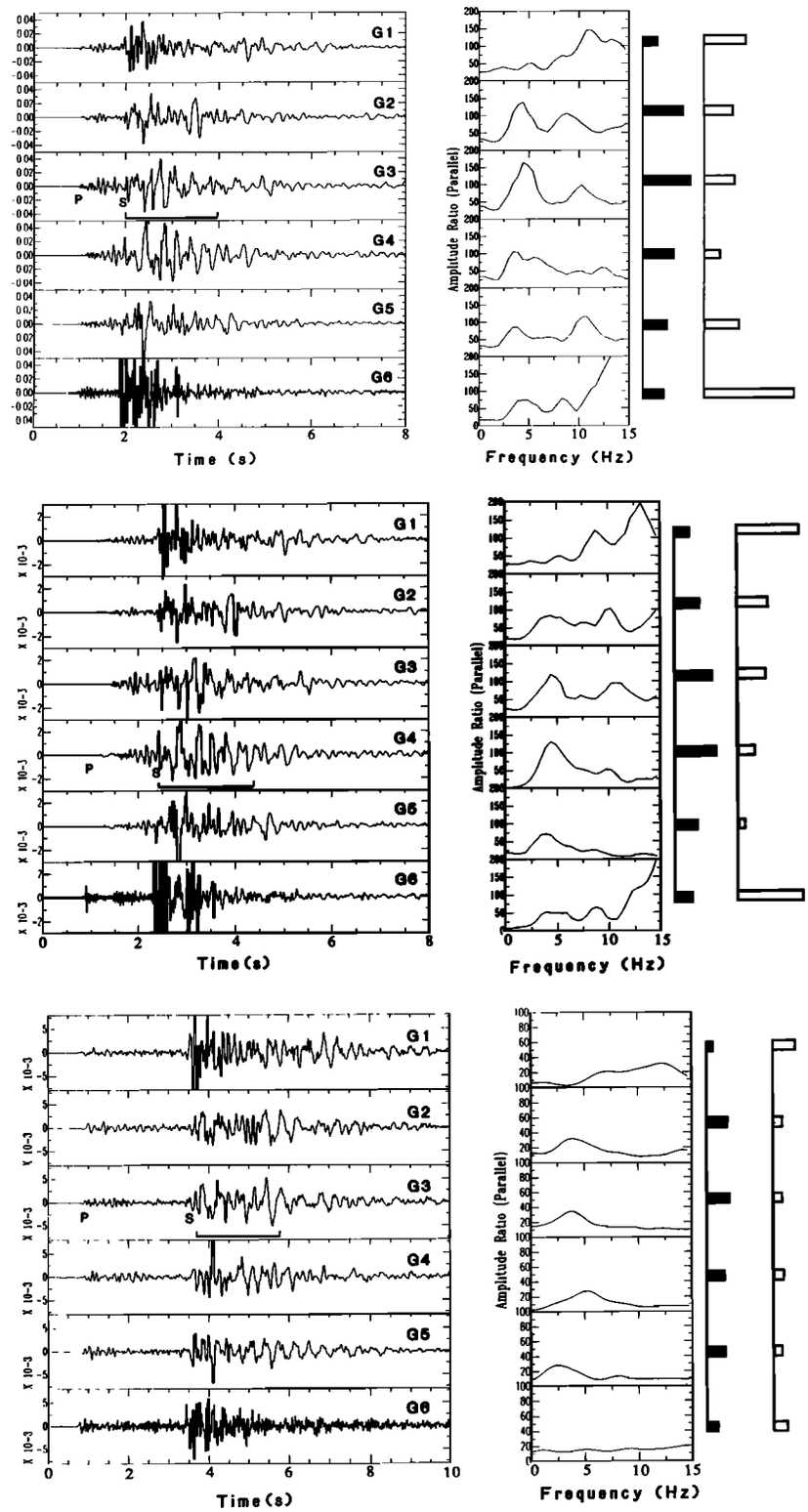

Figure 5. Horizontal components (parallel to the mainshock fault trace) of seismograms recorded at stations G1–G6 at site 8 for the three events 30, 27, and 26 with various hypocentral distances between the event and receiver site are shown from top to bottom. The normalized amplitude spectra are shown at the right of the seismograms. Notation as in Figure 4.

Evidence From a Dense Array Across the Fault Zone

A further confirmation of the existence of the fault zone trapped mode, as well as an accurate determination of the width of the low velocity zone (at least at Earth's surface), came from a joint experiment with the U.S. Geological Survey, in which we deployed 31 stations along a 2-km line lying perpendicular to the mainshock fault trace at site 8 as shown in Figure 7. Here, we shall present preliminary results from the experiment. Figure 8 shows vertical components of seismograms recorded by this array for the two aftershocks

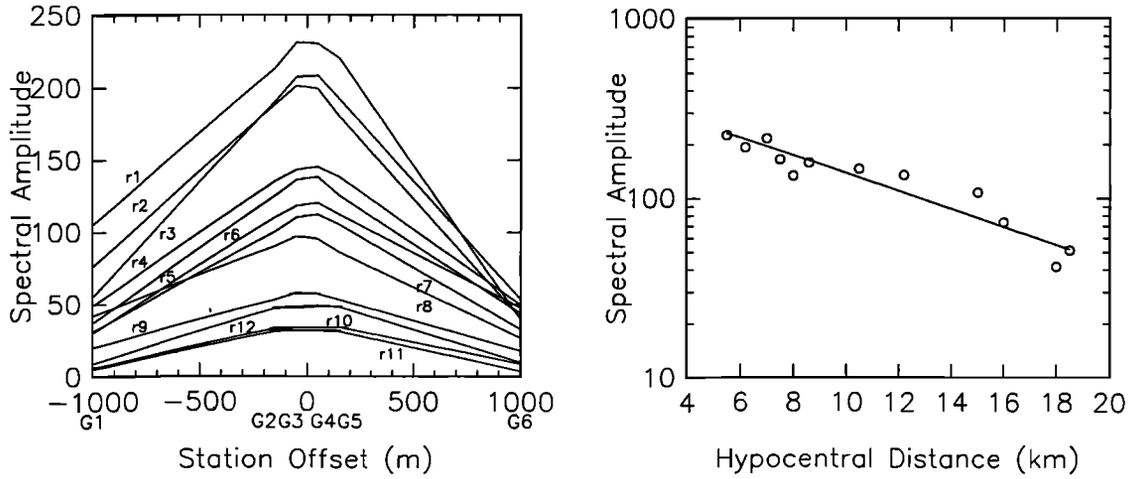

Figure 6. (left) The normalized peak spectral amplitudes of trapped modes at stations G1–G6 for 12 events are plotted as a function of station distances from the mainshock fault trace. Each curve comes from six peak amplitudes at G1–G6 for each event. The hypocentral distances for the 12 events, namely, r_{1-12}, are 5.5, 6.2, 7.0, 7.5, 8.0, 8.6, 10.5, 12.2, 15.0, 16.0, 18.0, and 18.5 km. (right) Spectral peaks at station G3 (or G4) for the 12 events are plotted as a function of hypocentral distance. Peak amplitudes have been multiplied by a factor of $(r_i/r_1)^{1/2}$, $i = 1, \cdots, 12$, to correct for geometrical spreading. The straight line is the least squares fit to the 12 peak amplitudes.

occurring within and outside the fault zone. One event was located at depth of 5.7 km and with an epicenter 3 km north of the array. We are confident that this event is located within or very close to the fault zone because of opposite polarities of the first P motions registered at stations located between W11 and W6 on the west side of the mainshock fault trace and stations located between W5 and E10 on the east side of the fault trace (see Figure 7 for station locations). We observed relatively long-period wave trains following the S waves at stations located between W5 and E5 near the mainshock fault trace. These wave trains diminish rapidly as the station offset from the fault trace increases. Further, no such long-period wave trains were recorded at any stations for the event occurring outside the fault zone (located at a depth of about 5 km and with epicenter about 3 km southwest of site 8) as shown on the right hand of Figure 8.

Figure 9 shows horizontal components (parallel to the fault trace) of seismograms for two more aftershocks occur-

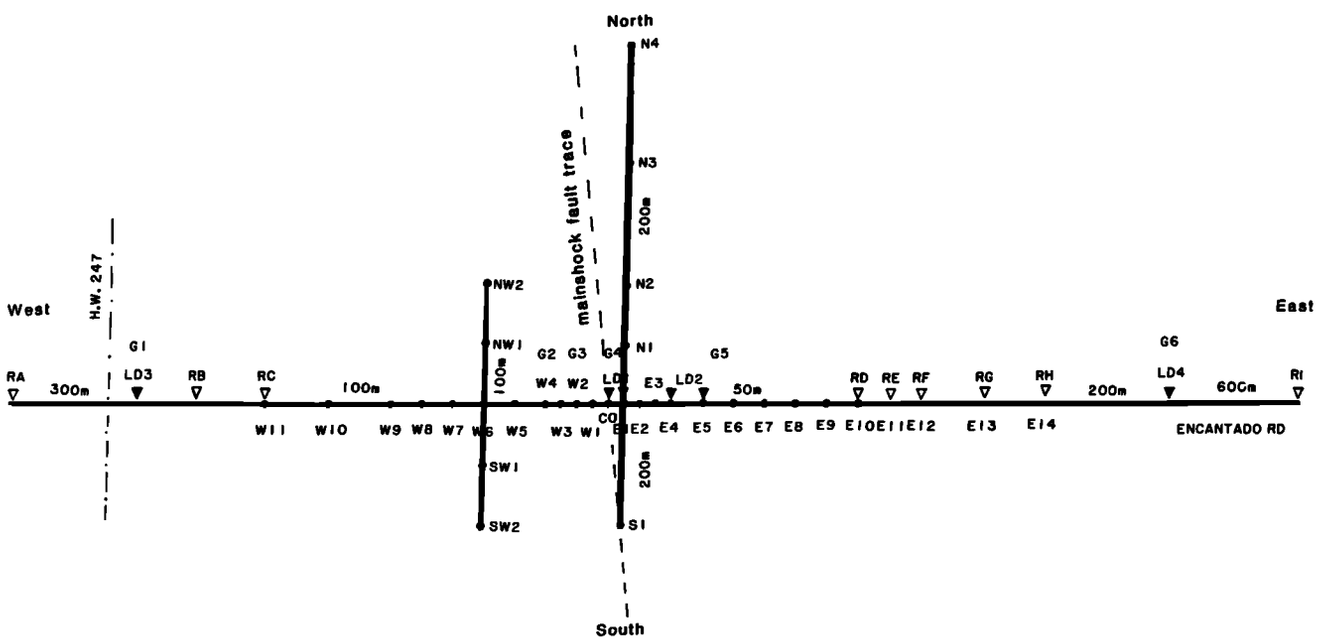

Figure 7. The map shows station locations of the dense array at site 8. W1–W11, C0, E1–E10, N1–N4, S1, NW1, NW2, SW1, and SW2 are PC recorder stations (solid dots). RA-I and LD1–LD4 are REFTEK stations with 2-Hz sensors (open triangles) and 1-Hz sensors (solid triangles), respectively. G1–G6 denote station positions of the mobile array as shown in Figure 3. The dashed line indicates the mainshock fault trace of the Landers earthquake.

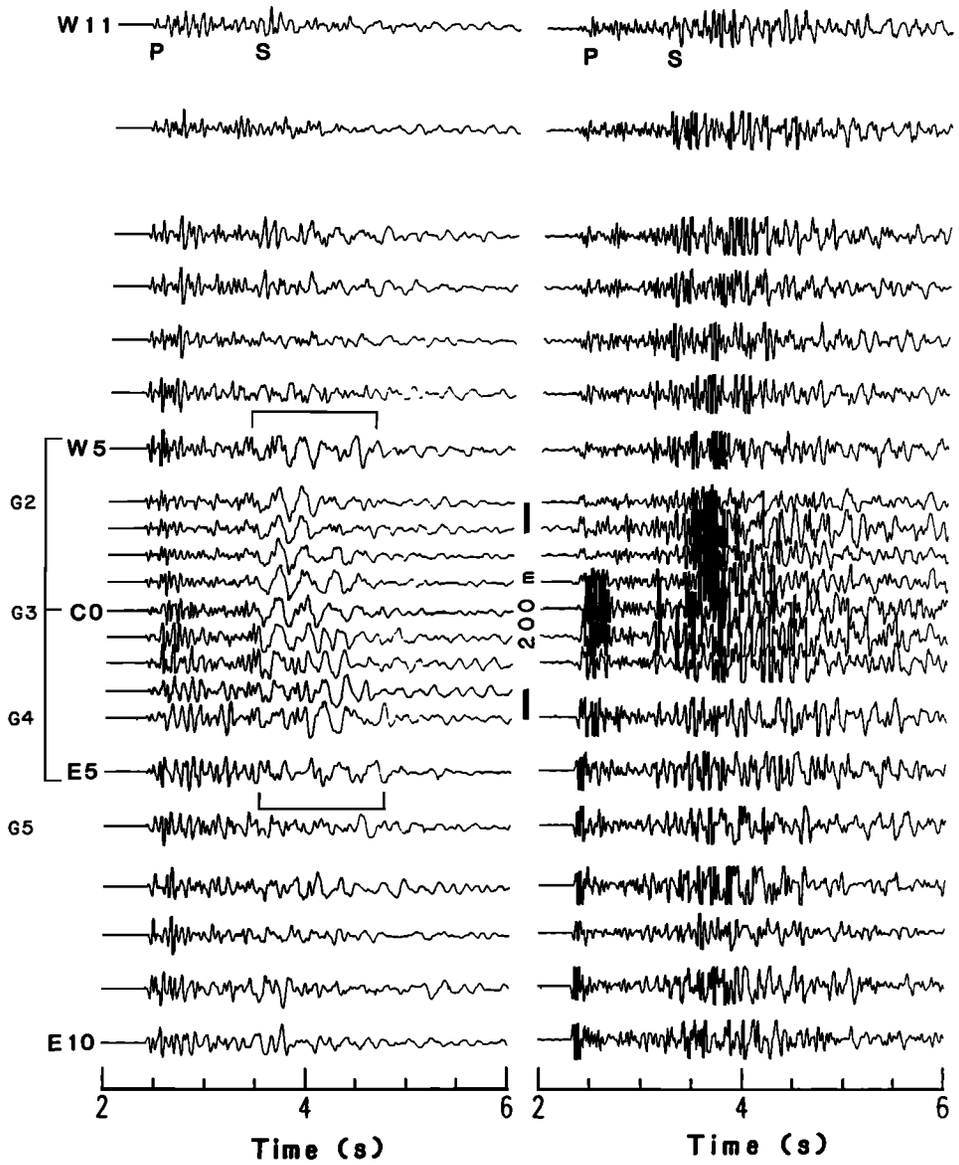

Figure 8. Vertical components of seismograms from the event occurring (left) within the fault zone and (right) outside the fault zone recorded at 21 stations of the dense array set up between W11 and E10 at site 8 (see Figure 7). The trace intervals correspond to spaces between stations at the site. The bracket between W4 and E5 indicates the distance range in which we observed clear trapped waves. G2–G5 denote station positions of the mobile array as shown in Figure 3.

ring within and outside the fault zone. The event that excited the trapped mode was located at a depth of 7 km, with an epicenter on the mainshock fault trace, 3 km south of site 8. The other event was located at depth of 6 km and 9 km southwest of site 8. Again, they confirm that fault zone trapped waves were clearly recorded at stations between W5 and E5 on or close to the mainshock fault trace. Since the distance between W5 and E5 is 300 m, we may conclude that the width of the low-velocity fault zone should be less than 300 m. The detailed structural parameters (including width and velocity) of the fault zone will be discussed in the following section.

Simulation of the Trapped Mode

We simulated fault zone trapped waves using a simple model composed of a low-velocity, low-Q layer sandwiched between two half-spaces with relatively high velocity and high Q. Using the phase shift method of *Li and Leary* [1990] and the formula for the Love wave part of the Green's function given by *Aki and Richards* [1980], we calculated synthetic trapped modes. The synthetic waveform consists of the fundamental and first higher mode Love-type waves.

We show three examples of the simulation of trapped waves. Figure 10 illustrates results from the simulation of the data recorded at stations GB and GC along the fault zone for event 20. Figure 11 illustrates results from the data recorded at stations G1–G6 across the fault zone for event 43 and from the data recorded at the dense seismic array for the event shown in the left side of Figure 8, respectively. We tested a range of model parameters (a fault width varying between 100 m and 300 m, phase velocity varying between 1.0 km/s and 2.5 km, and Q value varying between 20 and 100) to find

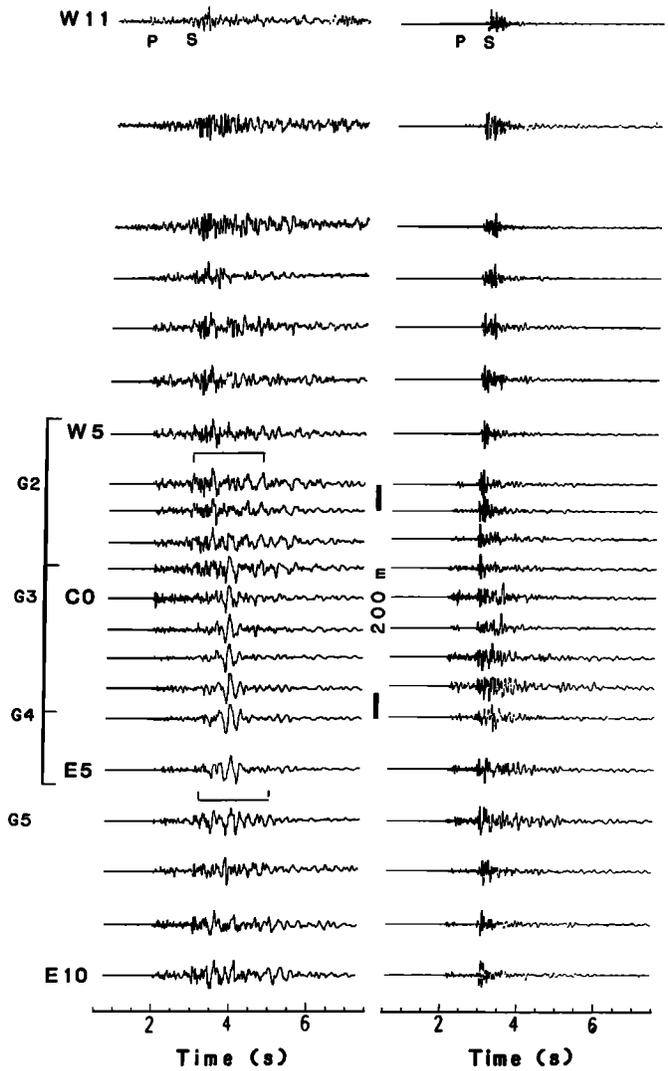

Figure 9. Horizontal components (parallel to the fault trace) of seismograms recorded at 21 stations of the dense array at site 8 for the two events occurring within the fault zone (left) and outside (right). Notation as in Figure 8.

trapped mode simulations best fitting the observations. These parameters are not very well constrained by this modeling because there is a trade-off among them. However, we think it is reasonable to constrain the velocities on the basis of observed S arrival times and the dispersive trapped waveforms. We obtained the best fit to observations using model parameters listed in Table 3: the width of the low-velocity fault zone is ~180 m, the shear velocity is 2.0–2.2 km/s and Q is ~50.

This result is somewhat restricted because we only used the trapped mode data from three events, and we also assumed the fault zone to be an infinite uniform waveguide. Interestingly, the width derived here agrees with the zone spanning all the traces of fault breaks during the Landers earthquake at site 8 as shown by the air photo in Figure 12. In fact, the stations between W5 and E5 of the dense array which recorded trapped modes bracket the observed fault traces.

A more thorough modeling of trapped waves from events listed in Table 2 should result in a more detailed 3-D models of the fault zone structure of the Landers earthquake than those considered here. This will be the subject of future work using numerical methods such as finite difference [e.g., *Vidale et al.*, 1985; *Helmberger and Vidale*, 1988; *Frankel and Vidale*, 1992] and/or boundary element method [e.g., *Hisada et al.*, 1993].

Distribution of Earthquakes With and Without Trapped Modes

Figure 13 (top) shows epicenters of aftershocks recorded at site 8, including 44 aftershocks from which we observed trapped modes and others without trapped waves. We found that epicenters of these 44 events are located on or close to the surface trace of the Landers earthquake, while the epicenters of events without trapped waves are either outside the mainshock fault zone or in or close to the fault zone but more distant than 20 km from site 8. Furthermore, the

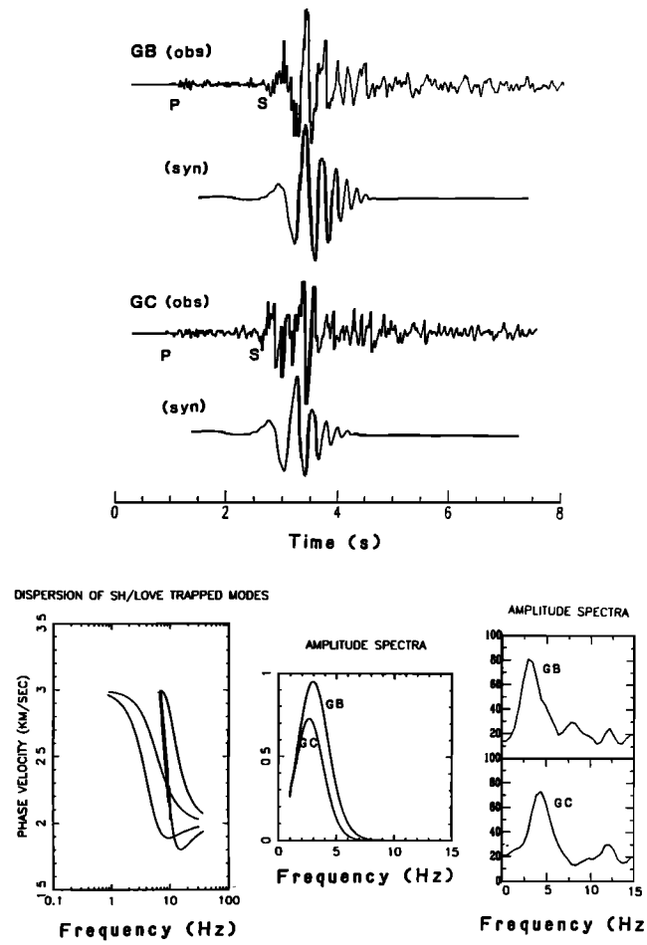

Figure 10. (top) Horizontal components (parallel to the fault trace) of seismograms recorded at stations GB and GC at site 8 for event 20 and synthetic SH-Love trapped mode waveforms using model parameters listed in Table 3. (bottom) Computed dispersion curves for the fundamental and the first high trapped modes, computed amplitude spectra of the fundamental mode at positions of GB and GC in response to a unit source located in the waveguide, and coda-normalized amplitude spectra of trapped waves observed at GB and GC.

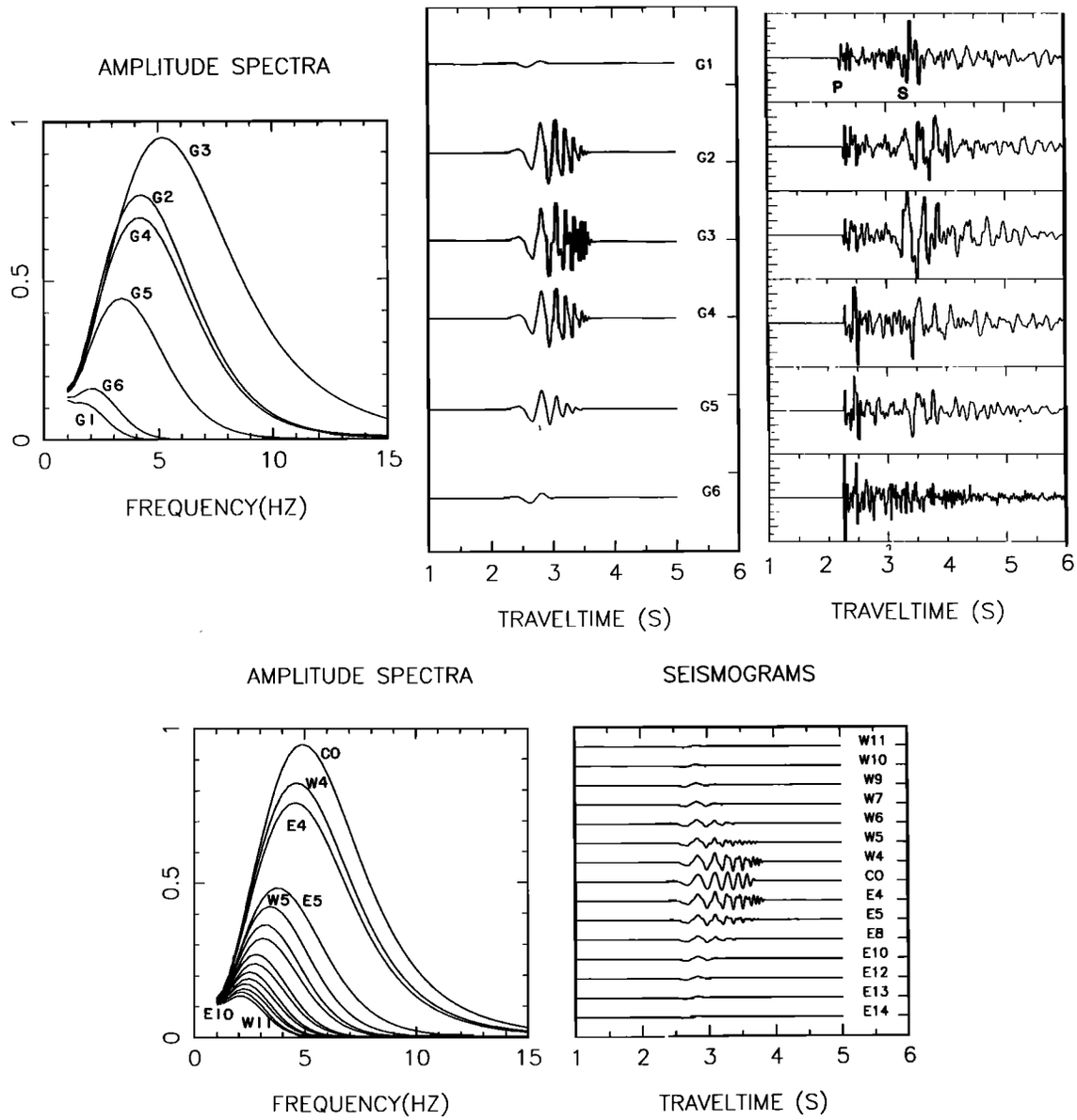

Figure 11. (top) From left to right, computed amplitude spectra of the fundamental mode and waveforms of trapped modes at positions of G1–G6 at site 8 for event 43 using model parameters listed in Table 3. Synthetic waveforms are consistent with observations. (bottom) Computed results from the simulation of trapped waves at the dense seismic array for the event which seismograms are shown on the left side of Figure 8.

locations of these 44 events are restricted to south of the fault bend where the fault starts to bend by 30° to the northwest direction. The focal depths of the events with trapped waves range from the near surface to a depth of about 10 km (Figure 13, bottom). This suggests that the low-velocity fault zone may extend from the surface to the depth of at least 10 km. The lateral distribution of epicenters with trapped waves suggests that the fault zone is continuous from the mainshock epicenter southward along the fault rupture plane beyond the Pinto Mountain Fault (PMF) that intersects the Landers fault.

As mentioned above, we observed trapped waves at site 8 from those events located south of the fault bend, but we did not observe them from those events with epicenters on the fault trace north of the fault bend. Some of those events are

Table 3. Fault Zone Waveguide Model Parameters as a Function of Source and Station Positions

Parameters	Event 20	Event 43	Event A
Width of LVFZ, m	180	180	180
Velocity of LVFZ, km/s	2.0	2.2	22
Q value of LVFZ	50	50	50
Velocity of surrounding rocks, km/s	3.0	3.0	3.0
Q value of surrounding rocks	200	200	200
Epicentral distance, km	6.0	1.5	5.0
Focal depth, km	10.6	6.3	5.5

Event A was recorded at the dense seismic array as shown at the left side of Figure 8. LVFZ, low-velocity fault zone.

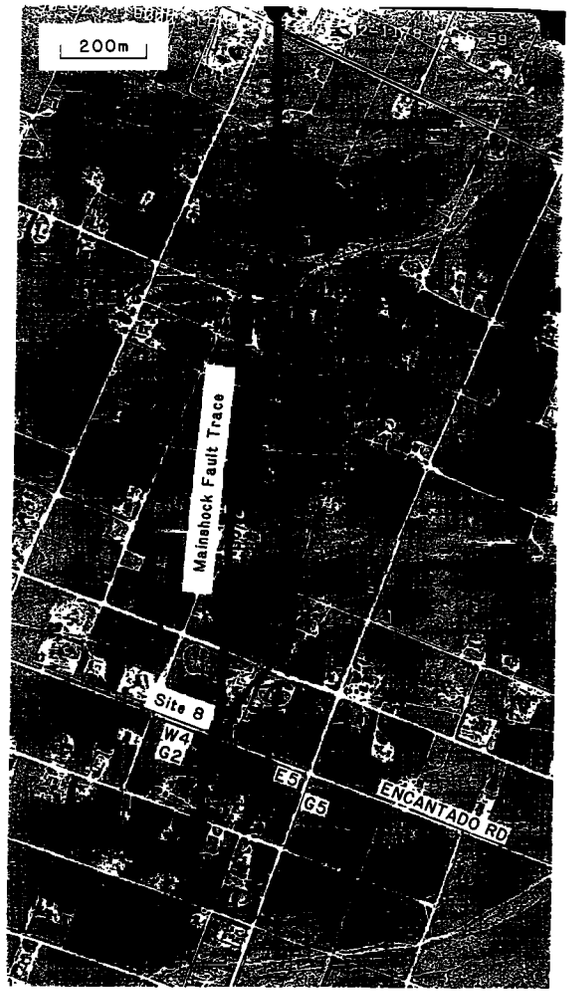

Figure 12. The air-photo map shows surface traces of the rupture of the Landers earthquake at site 8. G2 and G5 are station positions of the mobile array, and W4 and E5 are positions of PC stations.

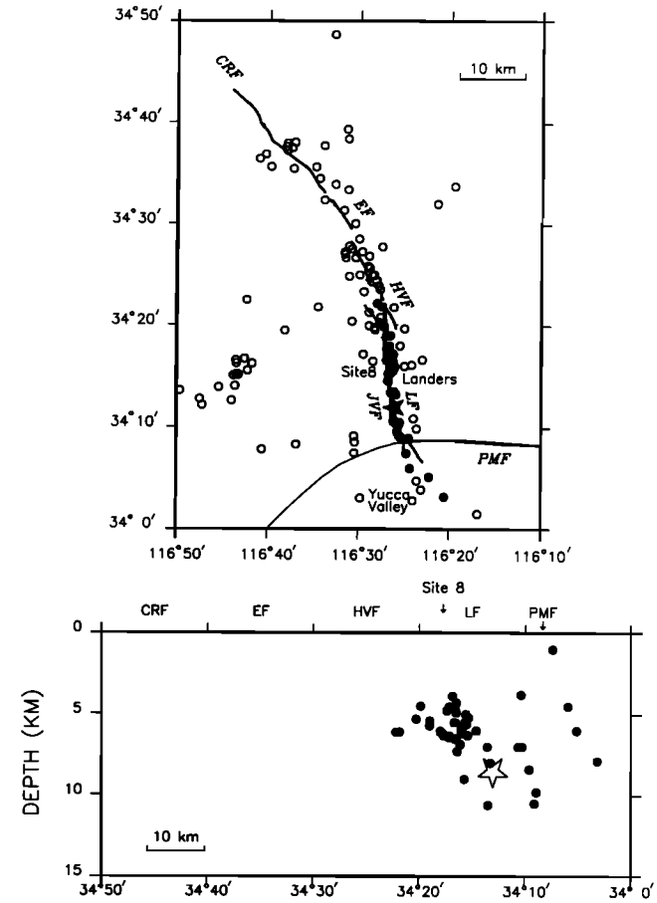

Figure 13. (top) The map shows epicenters of aftershocks recorded at site 8. Solid circles are events from which we observed trapped modes, while open circles are events without the trapped mode. CRF, Camp Rock Fault; EF, Emerson Fault; HVF, Homestead Valley Fault; JVF, Johnson Valley Fault; LF, Landers Fault; PMF, Pinto Mountain Fault. (bottom) Focal depths of aftershocks from which we observed trapped modes. The star denotes the $M7.4$ mainshock of the Landers earthquake of 1992.

located less than 20 km from site 8 so that trapped modes should be detectable at site 8 if they exist. Figure 14 shows seismograms recorded at site 8 from two aftershocks, one (event 38 in Table 2) occurring 6 km south of the fault bend and the other one with the epicenter (at 34°27.04′, 116°31.61′) 8 km north of the bend. Both epicenters are on the fault zone. We observed trapped waves at stations G2–G5 near the fault trace for the event occurring south of the fault bend. These trapped waves have a peak spectral amplitude in the frequency range 2–5 Hz, the same as previous examples. However, we did not observe such wave trains from the event occurring north of the fault bend. Stations G1–G6 recorded similar waveforms showing no spectral peaks at frequencies less than 5 Hz. This suggests that the fault zone waveguide may discontinue or become very narrow at the fault bend. Later, we shall address this question further using the data from site 3.

In contrast, we observed trapped waves from events occurring within the fault zone south of the intersection of the PMF and the fault trace of the Landers earthquake (14 km south of site 8). To confirm this, we shall show data from site 9 located at 3 km north of the PMF in the following section.

Evidence for the Trapped Mode at Site 9

In this section, we shall show evidence for trapped modes recorded by the mobile seismic array at site 9, 2.5 km south of the mainshock epicenter and 3 km north of the intersection of the PMF. Figure 15 shows results from two aftershocks occurring within and outside the fault zone. The event with the trapped mode (event 46 in Table 2) occurred at depth of 5.9 km and with the epicenter on the mainshock fault trace north of the intersection of the PMF. We observed convincing trapped modes from this event at stations G2–G4 near the mainshock fault trace (Figure 15, top). But such wave trains were not discernible at stations G1 and G6 at greater offsets from the fault trace. The coda-normalized spectra show large peaks at frequencies of 3–4 Hz for stations within the fault zone, while higher-frequency waves are more strongly attenuated within the fault zone than outside. The event without trapped modes was located at a depth of 3.2 km and with the epicenter (at 34°09.95′, 116°26.00′), 2 km southwest of site 9. We did not observe long-period wave trains following the S waves or any peaks

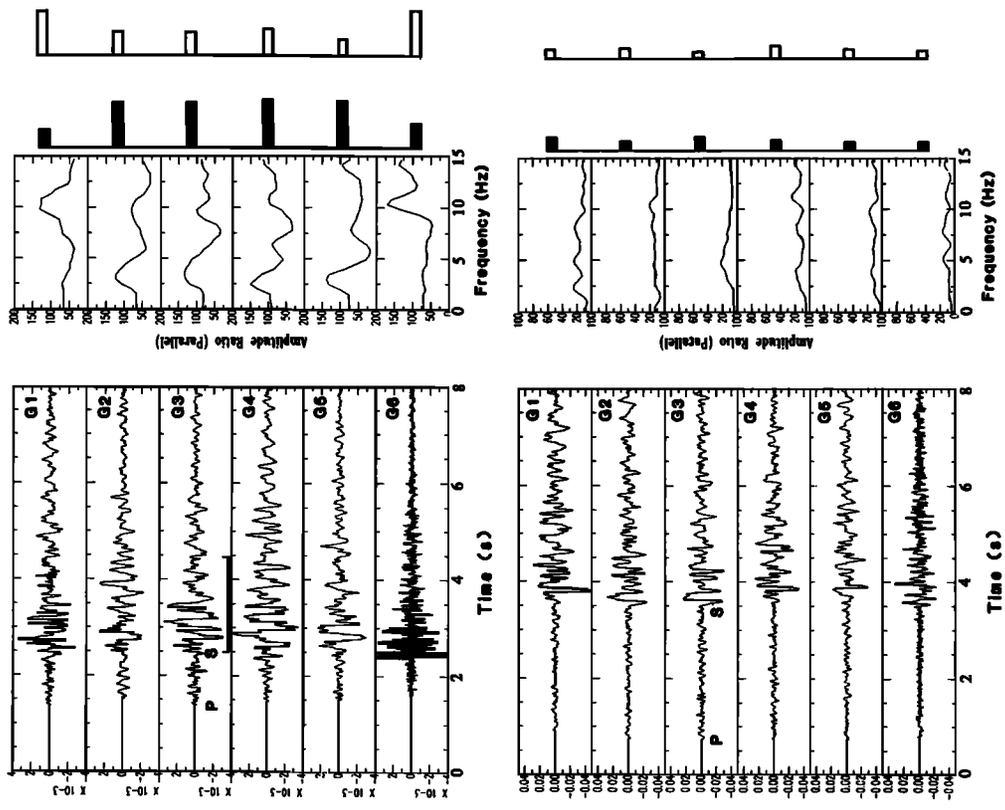

Figure 14. Horizontal components of seismograms (top) from event 38 for which we observed trapped modes at site 8 and (bottom) from the event occurring north of the fault bend, without trapped modes observed at site 8. The normalized amplitude spectra are shown at the right of the seismograms. Notation as in Figure 4.

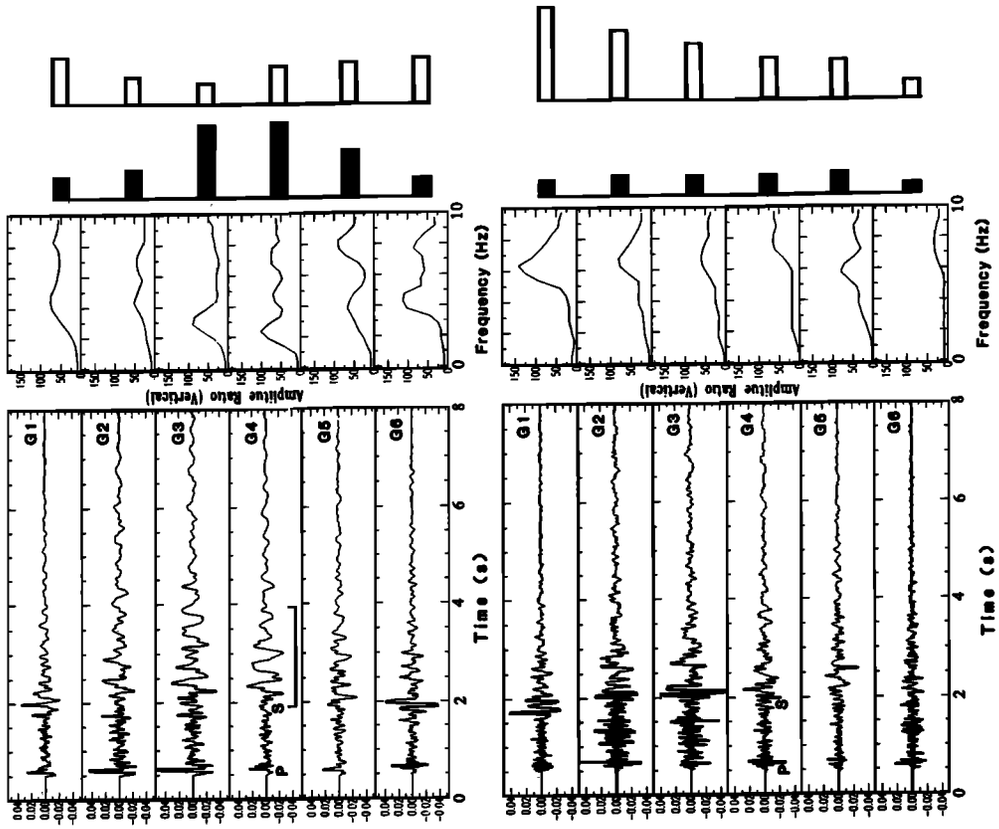

Figure 15. Vertical components of seismograms recorded at site 9 from two aftershocks occurring (top) within and (bottom) outside the fault zone north of the Pinto Mountain. The normalized amplitude spectra are shown at the right of the seismograms. Stations G1–G6 were set up at site 9 in the same configuration as at site 8. Notation as in Figure 4.

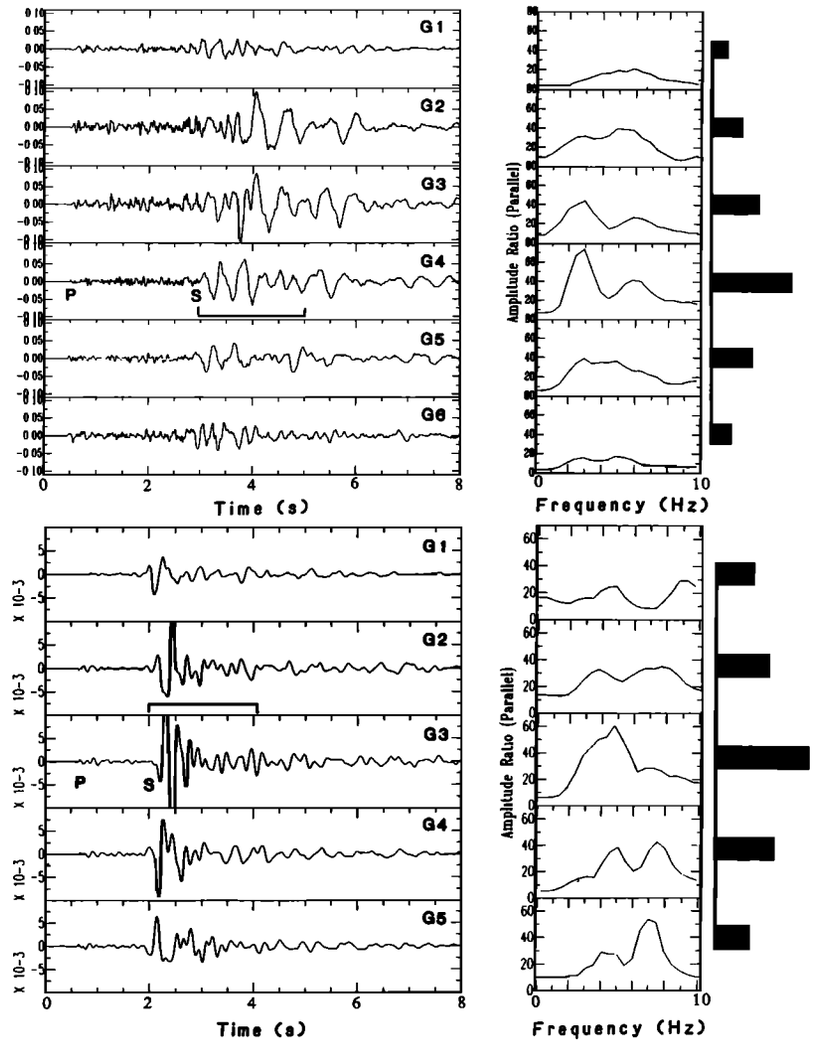

Figure 16. Horizontal components (parallel to the fault trace) of seismograms recorded at site 9 (top) from event 46 occurring within the fault zone south of the PMF and (bottom) from a deep event 68 occurring within the fault zone north of the PMF. The normalized amplitude spectra are shown at the right of the seismograms. Notation as in Figure 4.

in the spectral amplitudes at frequencies lower than 5 Hz at any of our stations (Figure 15, bottom). The spectral amplitude of high-frequency (about 6 Hz) waves systematically decays from stations G1–G6 because the source was located to the west of the seismic array.

Figure 16 illustrates two additional examples of trapped waves at site 9 (events 53 and 68 in Table 2) occurring within the fault zone; event 53 was located 10 km south of the PMF; event 68 was located near the mainshock epicenter north of the PMF. We observed clear trapped waves from both events. The relatively long-period, large-amplitude wave trains following *S* waves from event 53 were recorded at stations G2–G4 near the fault trace (Figure 16, top). The coda-normalized amplitude spectrum of these wave trains shows the peak value at frequencies of 2–5 Hz, similar as those shown for event 46 occurring north of the PMF. This provides additional evidence that the low-velocity fault zone extends continuously through the intersection of the PMF.

We also show results from event 68, which has the deepest focal depth (13.5 km) among the events from which we observed trapped waves at the Landers fault zone (Figure 16, bottom). The maximum spectral amplitude of trapped waves appeared at the frequency range 5–6 Hz, which is higher than 2–5 Hz observed for events occurring at shallower depths within the fault zone (e.g., events 46 and 53). These data suggest that the low-velocity fault zone may become narrower and/or the velocity contrast between the fault zone and surrounding rocks becomes smaller at depths greater than about 10 km.

Figure 17 shows the hypocentral distribution of events for which we identified trapped modes at site 9, providing evidence that the fault zone waveguide continues at depth across the Pinto Mountain fault.

Evidence for the Trapped Mode at Site 3

In early August 1992, we set up the seismic array across the mainshock fault trace at site 3 located 6 km north of the fault bend. Figure 18 shows seismograms from two earth-

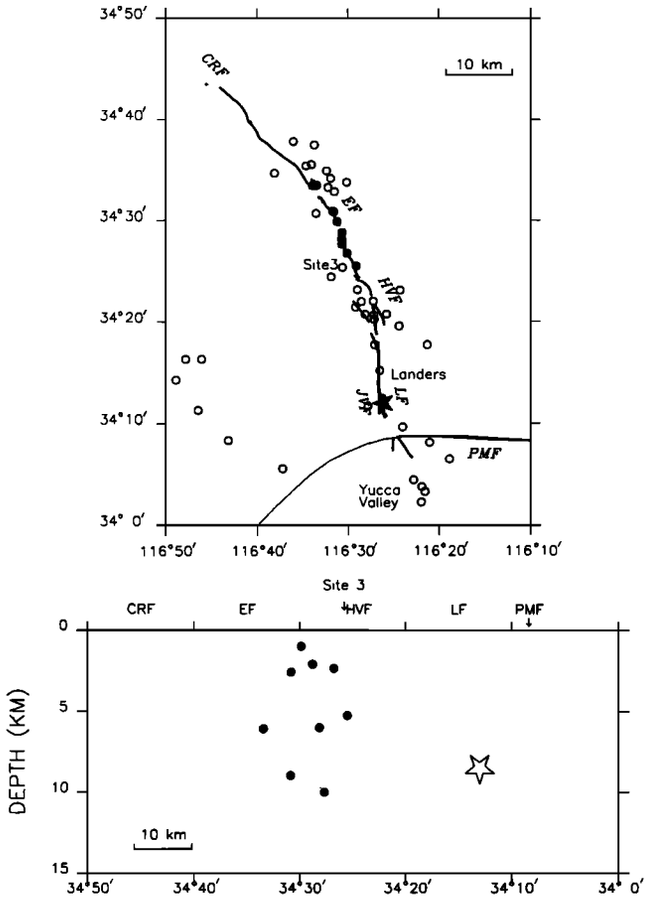

Figure 17. The map shows (top) epicenters and (bottom) focal depths of aftershocks recorded at site 9. Notation as in Figure 13.

quakes (events 78 and 76 in Table 2) occurring within the fault zone and with epicenters, 11 km and 2.5 km north of site 3, respectively. The epicenter of event 78 is located at depth of 8.9 km near the Galway Lake Road where the fault shows the maximum slip (about 7 m) on the surface. We observed trapped waves from this event at G3 and G4 located nearest the fault trace among the six stations (Figure 18, top). Station G3 registered the maximum amplitude of the coda-normalized spectrum of these wavetrains at 3 Hz, while the spectral peak decreases rapidly with the station offset from the fault trace. On the other hand, the high-frequency waves are strongly attenuated at G3. These data confirm the existence of the low-velocity fault zone along the rupture plane north of site 3.

The results shown at the bottom of Figure 18 also verify trapped waves excited by event 76 occurring close to the fault bend. The maximum normalized spectral amplitude of trapped waves from this event is at 5–6 Hz, relatively higher than that of event 78. We observed again that high-frequency (8–15 Hz) waves attenuate within the fault zone more strongly than outside. This event occurred on the Homestead Valley Fault which broke during the Landers earthquake north of the fault bend. At site 3 we did not obtain clear evidence for fault zone trapped waves from events occurring within the fault zone south of the fault bend. Figure 19 shows seismograms recorded at site 3 from the event located at depth of 8 km and with the epicenter (34°20.23′, 116°27.15′) south of the fault bend. We did not observe such long-period wave trains following S waves at any of our stations, as seen for event 78. These data again suggest that the fault zone is discontinuous or becomes very narrow at the bend.

Figure 20 shows the hypocentral distribution of events for which we clearly identified trapped modes at site 3. It is consistent with our previous conclusion that the fault zone waveguide is not continuous across the fault bend. The fault zone in this region could have a barrier, be very narrow, or be simply discontinuous.

Discussions and Conclusions

In this paper, we have described evidence for the existence of the fault zone trapped mode along the rupture plane of the Landers earthquake. These trapped modes appear as relatively long-period wave trains closely following S waves on seismograms recorded at stations located close to the mainshock fault trace for aftershocks occurring within the fault zone. They are clearer in the components parallel to the fault plane than normal to the fault plane. To find the propagation characteristic of the trapped mode, we used coda waves to normalize spectral amplitudes of these wave trains to a common source and receiver site condition.

The normalized amplitude spectra of these relatively long-period wave trains clearly show the presence of trapped modes with spectral peaks in the frequency range 3–4 Hz. The spectral peak amplitudes are largest for stations located in the fault zone and decay rapidly with the station offset from the fault trace. On the other hand, the amplitude spectra for high frequencies (between 8 and 15 Hz) show an increase in amplitude with the offset. We found that the normalized spectral amplitude attenuates systematically with hypocentral distance along the fault zone. The attenuation of the normalized amplitude with hypocentral distance was used to estimate Q of the fault zone at a specific frequency at which the trapped mode is dominant.

By comparing the observed waveform with the synthetic calculated for Love-type waves in a planar low-velocity and low-Q zone, we estimate a fault zone width of ~180 m, a fault zone shear velocity of 2.0–2.2 km/s, and a Q of ~50. Our estimation of the fault zone width is consistent with the zone containing the main and auxiliary fault breaks observed after the Landers earthquake at site 8 as shown by Figure 12. These results were further validated by the observations using a 31-station array set up perpendicular to the mainshock fault trace at site 8. This dense array clearly showed that the fault zone trapped waves were observable on seismograms recorded at stations located in the distance range of 300–400 m centered at the mainshock fault trace at site 8. This distance range is about twice the width of our fault zone model. Results from observations of trapped modes at the San Andreas fault near Parkfield using borehole seismic network data [*Li et al.*, 1990] and theoretical studies [*Ben-Zion and Aki*, 1990; *Li and Leary*, 1990] show that the trapped mode can be observed at distances up to 3 times the fault zone width.

The low-velocity, low-Q fault zone revealed by trapped modes may be the fault gouge layer within which the 1992 rupture occurred. Recently, *Marone and Kilgore* [1993] presented laboratory data showing that the critical slip

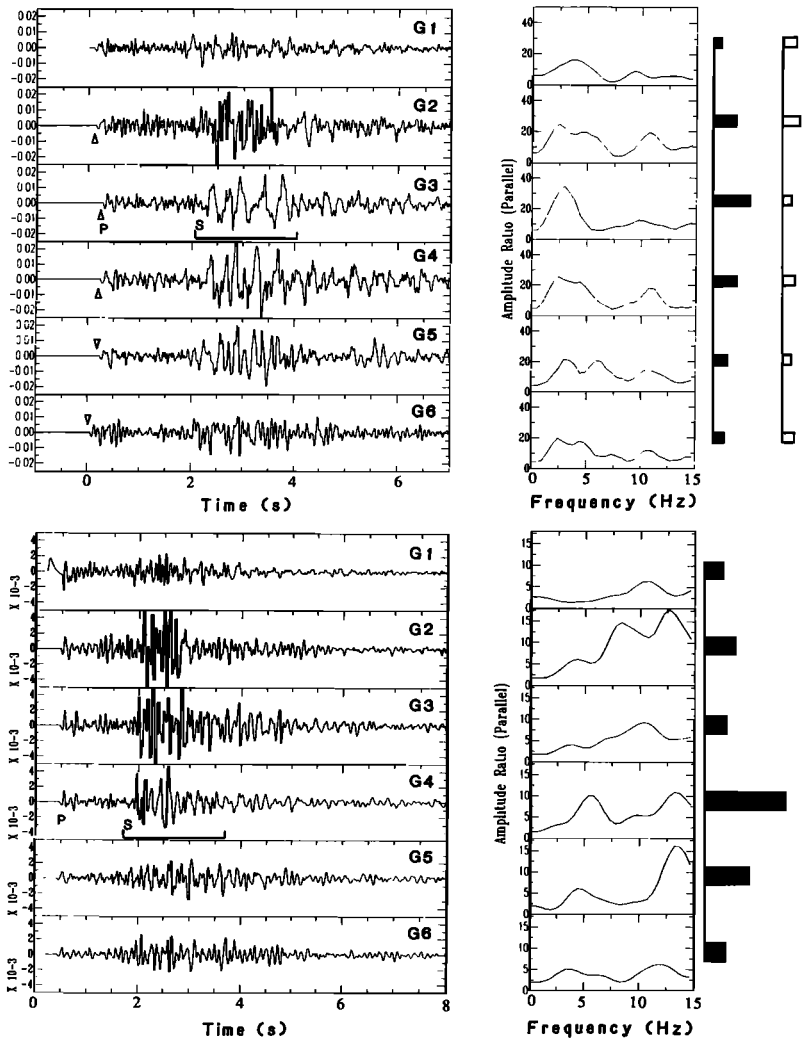

Figure 18. Vertical components of seismograms recorded at site 3 from two aftershocks (event 78 and 76 in Table 2) shown at top and bottom, respectively. The normalized amplitude spectra are shown at right of the seismograms. Stations G1–G6 were set up at site 3 in the same configuration as at site 8. Notation as in Figure 4.

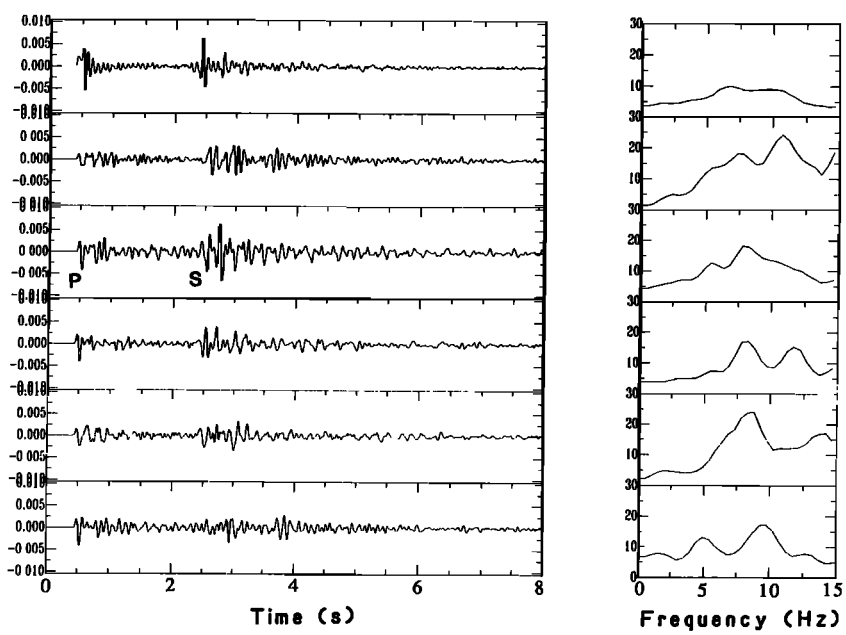

Figure 19. Horizontal components (parallel to the fault trace) of seismograms recorded at site 3 from event occurring within the fault zone south of the fault bend. Notation as in Figure 4.

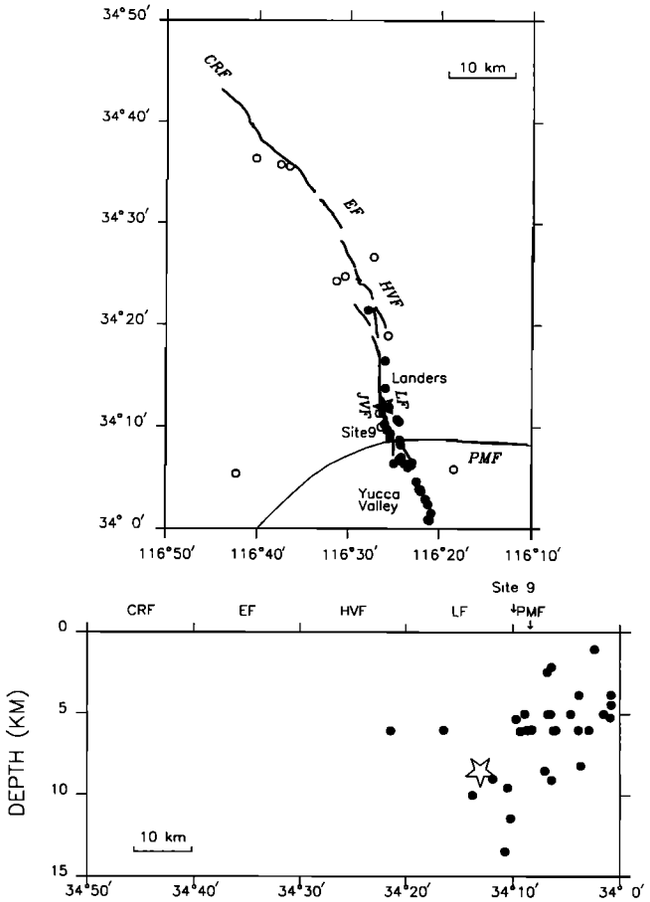

Figure 20. The map shows (top) epicenters and (bottom) focal depths of aftershocks recorded at site 3. Notation as in Figure 13.

distance D_c, over which strength breaks down during earthquake nucleation, scales with shear strain in simulated fault gouge. The experimental results offer an explanation why gouge zones of nature faults are commonly 10^2 to 10^3 m thick. According to the source model of *Papageorgiou and Aki* [1983a, b], the 180-m width of fault gouge resolved by trapped modes may correspond to the size of cohesive zone (break-down zone) acting as a spatial smoothing operator on fault slip. This width may be the inelastic thickness of the fault zone that causes the departure of the magnitude-frequency relations at very small magnitudes of earthquakes [*Rundle*, 1993]. This width may also be relevant to f_{max} estimated for major earthquakes in southern California [see *Chin and Aki*, 1991]. If this interpretation is correct, then we have the possibility to link in situ fault zone structural studies with earthquake source studies.

The hypocentral distributions of aftershocks for which we do or do not observe the trapped mode at sites 3, 8, and 9 suggest that the low-velocity fault zone along the rupture plane of the Landers earthquake may extend from the surface to a depth of at least 10 km, and may be continuous southward beyond the Pinto Mountain fault, possibly into two branches. The northern extent of this low-velocity fault zone is restricted at the fault bend, but we have evidence for the existence of the zone north of the fault bend. This is confirmed by the surface rupture of the Landers earthquake mapped along the Homestead Valley Fault and Emerson Fault north of the fault bend.

The existence of a discontinuity in the fault zone at the fault bend inferred by the trapped mode data is also supported by results from source inversion studies of telemetric and strong motion records [*Ammon et al.*, 1993; *Campillo and Archuleta*, 1992; *Dreger and Helmberger*, 1992; *Kanamori et al.*, 1992; *Wald et al.*, 1992] and the surface offsets mapped in the field [*Sieh*, 1992; *Staff of the U.S. Geological Survey*, 1992]. The slip distribution determined with the empirical Green's function method for near-field strong motion data indicates that the Landers earthquake consists of two distinct subevents separated at the fault bend [*Kanamori et al.*, 1992], consistent with the fault zone structure determined from our trapped mode data. However, *Hough et al.* [1993] found that the mapped surface rupture south of the Pinto Mountain fault (PMF) was associated with a *M*5.7 aftershock occurring 3 min after the mainshock and with an epicenter about 3 km south of the PMF. This aftershock caused a rupture length of 11 km and the maximum displacement 20 cm. They suggest that the left-lateral east-west trending PMF played a significant role in segmenting the "Landers" rupture. On the other hand, our trapped mode data recorded about 1 month after the Landers earthquake suggests the continuity of the rupture plane at depth beyond the PMF.

Acknowledgments. This study is supported by the Southern California Earthquake Center (SCEC) under National Science Foundation grant EAR-8920136 and U.S. Geological Survey grant 14-0A-0001-A0899, and partially supported by the U.S. Department of Energy under grant DE-FG03-87ER13807. We greatly appreciate the IRIS center for the usage of PASSCAL instruments in the USGS/USC joint experiment. We would like to thank Kevin Mayeda for his kind help with using the SAC software and James Moore for his fault trace data. We are also grateful to Randy White, David Harlow, Steve Maichnick, and Bob Westerlund from the USGS, and Robert Banfill participated in our joint experiment. We appreciate the useful discussions with John Vidale and Paul Spudich on the simulation and interpretation of the data. We also thank an anonymous reviewer and the associated editor for their critical comments on our original manuscript. This paper is SCEC publication 29.

References

Aki, K., Analysis of the seismic coda of local earthquakes as scattered waves, *J. Geophys. Res.*, *74*, 615–631, 1969.

Aki, K., and P. C. Richards, *Quantitative Seismology*, W. H. Freeman, New York, 1980.

Ammon, C. J., A. A. Velasco, and T. Lay, Rapid estimation of rupture directivity: Application to the 1992 Landers (M_s = 7.4) and Cape Mendocino (M_s = 7.2) California earthquakes, *Geophys. Res. Lett.*, *20*, 97–100, 1993.

Anderson, J., and S. E. Hough, A model for the shape of the Fourier amplitude spectrum of acceleration at high frequencies, *Bull. Seismol. Soc. Am.*, *74*, 1969–1993, 1984.

Ben-Zion, Y., and K. Aki, Seismic radiation from an *SH* line source in a laterally heterogeneous planar fault, *Bull. Seismol. Soc. Am.*, *80*, 971–994, 1990.

Brune, J. N., Tectonic stress and the spectra of seismic shear waves from earthquakes, *J. Geophys. Res.*, *75*, 4997–5009, 1970.

Campillo, M., and R. Archuleta, A rupture model for the 28 June, 1992 Landers, California, earthquake (abstract), *Eos Trans. AGU*, *73*(43), Fall Meeting suppl., 374, 1992.

Chin, B. H., and K. Aki, Simultaneous study of the source, path and site effects on strong ground motion during the 1989 Loma Prieta earthquake: A preliminary result on pervasive non-linear site effects, *Bull. Seismol. Soc. Am.*, *81*, 1859–1884, 1991.

Chouet, B., Source, scattering and attenuation effects on high

frequency seismic waves, Ph.D. thesis, Mass. Inst. of Technol., Cambridge, 1976.

Dreger, D. S., and D. V. Helmberger, Constraints on source directivity and slip distribution for the Landers earthquake from TERRAscope low gain data (abstract), *Eos Trans. AGU*, *73*(43), Fall Meeting suppl., 373, 1992.

Frankel, A. S., and J. E. Vidale, A three-dimensional simulation of seismic waves in the Santa Clara Valley, California, from a Loma Prieta aftershock, *Bull. Seismol. Soc. Am.*, *82*, 2045–2074, 1992.

Hanks, T. C., F_{max}, *Bull. Seismol. Soc. Am.*, *72*, 1867–1879, 1982.

Helmberger, D. V., and J. E. Vidale, Modeling strong motions produced by earthquakes with two-dimensional numerical codes, *Bull. Seismol. Soc. Am.*, *78*, 109–121, 1988.

Hisada, Y., K. Aki, and T. L. Teng, 3-D simulation of surface wave propagation in the Kanto sedimentary basin, Japan, 2, Application of the surface wave BEM, *Bull. Seismol. Soc. Am.*, *83*, 1700–1720, 1993.

Hough, S. E., J. Mori, E. Sembera, G. Glassmoyer, C. Mueller, and L. Wennerberg, The southern "Landers" surface rupture (abstract), *Eos Trans. AGU*, *74*(16), Spring Meeting suppl., 215, 1993.

Ida, Y., The maximum acceleration of seismic ground motion, *Bull. Seismol. Soc. Am.*, *63*, 959–968, 1973.

Kanamori, H., H. K. Thio, D. Dreger, E. Hauksson, and T. Heaton, Initial investigation of the Landers, California, earthquake of 28 June 1992 using TERRAscope, *Geophys. Res. Lett.*, *19*, 2267–2270, 1992.

Kinoshita, S., Local characteristics of the f_{max} of bedrock motion in Tokyo metropolitan area, Japan, *J. Phys. Earth*, *40*, 487–515, 1992.

Leary, P. C., Y.-G. Li, and K. Aki, Observation and modeling of fault zone fracture seismic anisotropy, I, *P*, *SV*, *SH* travel times, *Geophys. J. R. Astron. Soc.*, *91*, 461–484, 1987.

Lee, W. H. K., Toolbox for seismic data acquisition, processing, and analysis, *IAPEI Software Libra.*, *1*, Seismol. Soc. of Am., El Cerrito, Calif., 1989.

Li, Y.-G., and P. C. Leary, Fault zone trapped seismic waves, *Bull. Seismol. Soc. Am.*, *80*, 1245–1271, 1990.

Li, Y.-G., P. C. Leary, and K. Aki, Observation and modeling of fault zone fracture seismic anisotropy, II, *P*-wave polarization anomalies, *Geophys. J. R. Astron. Soc.*, *91*, 485–492, 1987.

Li, Y.-G., P. C. Leary, K. Aki, and P. E. Malin, Seismic trapped modes in the Oroville and San Andreas fault zones, *Science*, *249*, 763–766, 1990.

Marone, C., and B. Kilgore, Scaling of the critical slip distance for seismic faulting with shear strain in fault zones, *Nature*, *362*, 618–621, 1993.

Mayeda, K., S. Koyanagi, M. Hoshiba, K. Aki, and Y. Zeng, A comparative study of scattering, intrinsic, and coda Q^{-1} for Hawaii, Long Valley, and central California between 1.5 and 15.0 Hz, *J. Geophys. Res.*, *97*, 6643–6659, 1992.

Papageorgiou, A. S., and K. Aki, A specific barrier model for the quantitative description of inhomogeneous faulting and the prediction of strong motion, I, Description of the model, *Bull. Seismol. Soc. Am.*, *73*, 693–722, 1983a.

Papageorgiou, A. S., and K. Aki, A specific barrier model for the quantitative description of inhomogeneous faulting and the prediction of strong motion, II, Applications of the model, *Bull. Seismol. Soc. Am.*, *73*, 953–978, 1983b.

Phillips, W. S., The separation of source, path and site effects on high frequency seismic waves: An analysis using coda wave techniques, Ph.D. thesis, Mass. Inst. of Technol., Cambridge, 1985.

Rundle, J. B., Magnitude-frequency relations for earthquakes using a statistical mechanical approach, *J. Geophys. Res.*, *98*, 21,943–21,949, 1993.

Sieh, K., Surficial fault ruptures associated with the June 28, 1992 Landers earthquake, California, paper presented at the Monthly Seminar of the Southern California Earthquake Center, Univ. of South. Calif., Los Angeles, Aug. 27, 1992.

Staff of the U.S. Geological Survey, Pattern of surface rupture associated with the June 28, 1992, Landers earthquake (abstract), *Eos Trans. AGU*, *73*(43), Fall Meeting suppl., 357, 1992.

Su, F., K. Aki, T. Teng, Y. Zeng, S. Koyanagi, and K. Mayeda, The relation between site amplification factor and surficial geology in central California, *Bull. Seismol. Soc. Am.*, *82*, 580–602, 1992.

Tucker, B. E., and J. L. King, Dependence of sediment-filled valley response on input amplitude and valley properties, *Bull. Seismol. Soc. Am.*, *74*, 153–165, 1984.

Vidale, J. E., D. H. Helmberger, and R. W. Clayton, Finite difference seismograms for *SH* waves, *J. Geophys. Res.*, *75*, 1765–1782, 1985.

Wald, D. J., H. K. Thio, D. Dreger, and T. H. Heaton, On developing a single rupture model for the 1992 Landers, California earthquake consistent with static, broadband teleseismic, regional and strong-motion data sets (abstract), *Eos Trans. AGU*, *73*(43), Fall Meeting suppl., 358, 1992.

D. Adams, K. Aki, A. Hasemi, and Y.-G. Li, Department of Earth Sciences, University of Southern California, University Park, Los Angeles, CA 90089. (e-mail: Internet ygli@coda.usc.edu)

W. H. K. Lee, U.S. Geological Survey, 345 Middlefield Road, MS 977, Menlo Park, CA 94025. (e-mail: Internet lee@andreas.wr.usgs.gov)

(Received January 22, 1993; revised August 23, 1993; accepted February 11, 1994.)